CHEMISTRY OF MATERIALS

pubs.acs.org/cm

Article

Total Scattering Study of Local Structural Changes in $MnAs_{1-x}P_x$ Influenced by Magnetic Interactions

Dipankar Saha,* Susmit Kumar, Bruno Gonano, Anja Olafsen Sjåstad, and Helmer Fjellvåg*

Cite This: *Chem. Mater.* 2021, 33, 2576−2584

Read Online

ACCESS | Metrics & More | Article Recommendations | Supporting Information

ABSTRACT: The interplay between fluctuations of the local structure and magnetic interactions is of great importance for phenomena like superconductivity, colossal magnetoresistance, and frustrated magnetism. Such local distortions are often subtle and difficult to probe. The metallic $MnAs_{1-x}P_x$ (x = 0.06, 0.12, 0.18) solid solution represents a sensitive model system, currently analyzed by variable-temperature X-ray total scattering (TS). A second-order transition (*Pnma* to $P6_3/mmc$) occurs on heating, intimately coupled to magnetic ordering at low temperatures and a temperature-induced low- to high-spin transition for manganese. Intrinsic compositional fluctuations along with a particular magneto-volumetric coupling to low- and high-spin like states triggers formation of local high-symmetry nanosized domains in an orthorhombically deformed matrix that eventually converts globally into a high-temperature hexagonal arrangement. These features are only traced by TS analyses, whereas diffraction provides a regular second-order transition with, e.g., cationic displacements defined by Rietveld analysis acting as order parameter. The coexistence model provides good fits of the TS data and, on average, translates nicely into a continuous $V(T)$ thermal expansion relation with maximum expansivity in the range where the TS data shows the largest difference between local (<20 Å) and intermediate-range (20−80 Å) structures. The degree of local distortions, $Mn(As, P)_6$ octahedra inclusive, is a result of volume-dependent electronic properties as well as magnetic interactions. This study demonstrates how X-ray TS can conveniently give essential insights into the local symmetry fluctuations from the perspective of strong magnetic interactions.

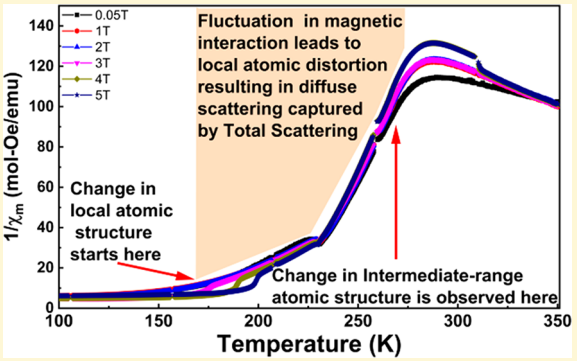

INTRODUCTION

Nanoscale heterogeneities, structural variations, and broken symmetry states play a ubiquitous role in emergent properties such as colossal magnetoresistance,[1] frustrated magnetism,[2,3] pseudogaps,[4] and high-temperature superconductivity.[5,6] The properties of these types of complex materials depend critically on local deviations from the long-range average structure. For example, magnetic fluctuations are considered to be responsible for slowing down the pseudogap phase of the high-temperature superconductor $YBa_2Cu_3O_y$ ($6.72 < y < 6.95$).[7] Variations in the local magnetic moments are a result of not only the exchange interactions with their neighbors but also the local effective crystal fields. The latter becomes prominent if the (anion) substructure contains atoms A and B with different effective charges. Therefore, each magnetic atom will experience a local low-symmetry crystal field in addition to the average crystal field arising from the crystal structure.[8] This random anisotropy may, in turn, influence the local atomic structure. Moreover, during a magnetic ordering transition (MT), the local change in magnetic interactions might influence the local atomic structure without entering into the situation of a simultaneous atomic structural phase transition (ASPT). Such a change in local structure will result in diffuse scattering that cannot be analyzed by conventional crystallographic methods based solely on Bragg reflections. However, in total scattering (TS) methods the diffuse scattering is analyzed in parallel with Bragg scattering on an equal basis.[9] TS has, for instance, been successfully utilized to show co-emergence of magnetic order and structural fluctuations in magnetite below the Curie transition.[10]

In the current article, we probe the change in the local atomic structure during a continuous magnetostructural phase transition in magnetocaloric $MnAs_{1-x}P_x$ (x = 0.06, 0.12, 0.18). There is recently a strong renewed interest in MnP and related transition metal pnictides with MnP-type orthorhombic structure due to the discovery of unconventional superconductivity under high pressure and upon chemical substitution.[11] The superconductivity is considered to arise from an enhanced coupling of (helimagnetic) spiral spin fluctuations and indicates that superconductivity and magnet-

Received: January 13, 2021
Revised: March 8, 2021
Published: March 18, 2021

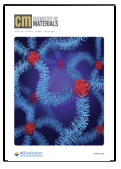

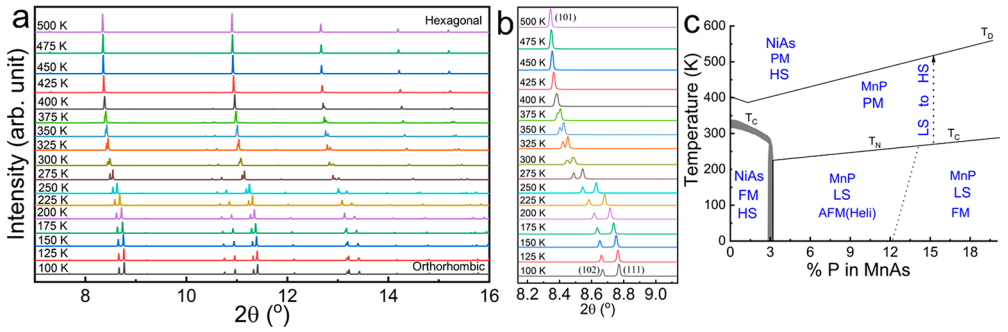

Figure 1. (a) Variable-temperature PXRD data of $MnAs_{0.94}P_{0.06}$. (b) Zoomed view of the main PXRD peak to illustrate the second-order phase transition. (c) Schematic phase diagram for $MnAs_{1-x}P_x$. NiAs and MnP have hexagonal ($P6_3/mmc$) and orthorhombic($Pnma$) structure, respectively. T_D transition temperature for the transition between MnP- and NiAs-type structure. T_N and $T_c$are the Néel and Curie temperatures. PM, FM, and AFM represent the paramagnetic, ferromagnetic, and antiferrmagnetic structures, respectively. HS and LS stand for high-spin ans low-spin structure.

ism are intertwined. Fluctuation and competition between phonons and spin appear to have a direct connection to a superconducting pairing of s, p, and d character. In this context, the variation of the pitch of the incommensurate helical fluctuations provides rich grounds for local FM and intermediate-range AFM orders. On the other hand, in MnP-type CrAs, the unconventional pressure-induced superconductivity is achieved by shifting the quantum critical point (QCP) by Al substitution.[12]

Magnetostructural phase transitions may be accompanied by substantial magnetocaloric (MC) effects that possibly can be exploited for room-temperature refrigeration.[13,14] MnAs and ternary derivatives show promising behavior for such room-temperature applications.[15,16] The transition temperature for the ordering of magnetic moments is affected by the local coordination (composition, symmetry). Furthermore, the ordering process is characterized by magnetic entropy changes (ΔS_M) across the phase transition. A giant MC effect occurs when the first-order ASPT couples with the magnetic transition. MnAs exhibits this behavior, where the first-order magnetostructural transition temperature is T_C = 318 K[17] and occurs between a low-temperature ferromagnetic (FM) hexagonal NiAs-type phase (space group $P6_3/mmc$) and an orthorhombic paramagnetic (PM) MnP-type phase ($Pnma$).[18] Substituting As with phosphorus P ($MnAs_{1-x}P_x$, x = 0.06, 0.12, and 0.18) allows the MnP-type phase to stabilize at ambient conditions. The phase diagram for $MnAs_{1-x}P_x$ is shown in Figure 1c. On increasing temperature, a second-order MnP−PM to NiAs−PM transition occurs, increasing from 425 K for x = 0.06 to 500K for x = 0.18. This symmetry-allowed displacive transition takes place over a wide temperature range.[19] In the orthorhombic regime, the MT is decoupled from ASPT and occurs at 230, 241, and 245 K for x = 0.06, 0.12, and 0.18, respectively. Importantly, thermal expansivity and magnetic susceptibility data along with paramagnetic diffuse scattering data measured by powder neutron scattering reveal a continuous low- to high-spin conversion for the Mn sublattice (assuming Mn^{3+} in the ionic limit; from S = 1 to S = 2) of $MnAs_{1-x}P_x$.[20]

The $MnAs_{1-x}P_x$ system is perfectly suited for exploring how the local structure influences the magnetic spin transition and, thereby the structural phase transition from $Pnma$ to $P6_3/mmc$. The average Mn spin state appears to be very dependent on bond distances (unit cell volume; distortions). Hence, this makes it possible to explore how distortions in the local symmetry owing to quite different Mn−As and Mn−P bond distances affect the magnetism and structure. We address this challenging issue by means of a total scattering analysis of $MnAs_{1-x}P_x$ and correlate the findings with magnetic susceptibility data.

EXPERIMENTAL SECTION

The powder samples of $MnAs_{1-x}P_x$ (x = 0.06, 0.12, 0.18) were prepared as earlier described.[19] The purity and homogeneity of the samples were ascertained from powder X-ray diffraction (PXRD) data recorded using a Bruker D8 Discover diffractometer with Bragg−Brentano geometry, Cu Kα1 radiation [λ = 1.540598 Å; Ge (111) monochromator], and a LynxEye detector. Total scattering PDF data were collected at the Materials Science Beamline[21] at the Swiss Light Source (SLS; Paul Scherrer Institut, Villigen). Silicon was used as a calibrant for wavelength and instrumental parameters (a_{Si} = 5.431194 Å at 22.5 °C, NIST powder diffraction standard 640c). The diffractometer was operated in Debye−Scherrer geometry with a Mythen microstrip detector and capillary spinner. The wavelength was 0.406080 Å. The Mythen microstrip detector was placed at four different 2Θ positions in order to collect a full set of angular data extending to high Q_{max} for the subsequent PDF analysis. Samples were packed under Ar atmosphere in a 0.3 mm diameter quartz capillary and sealed to avoid any oxygen/moisture in the capillary. A liquid nitrogen flow cryostat from Oxford was used in the temperature range from 100 to 500 K. Data were collected at 25 K intervals; the total collection time at each temperature was 40 min. The diffraction data were normalized and reduced by standard routines at the beamline. The xPDFsuite[22,23] was used for Fourier transformation of the total scattering structure function $S(Q)$ to obtain the PDF. Q_{min} = 0.5 Å^{-1} and Q_{max} = 28 Å^{-1} were used for the Fourier transformation. Experimental resolution parameters Q_{damp} = 0.0038 and Q_{broad} = 0.00229 were determined through refinements of PDF data for the Si standard. Unit cell parameters, anisotropic thermal factors, delta 2, and symmetry-allowed positions (space groups = $Pnma$ and $P6_3/mmc$) were refined to give the best fit to the experimental data. Rietveld refinements were carried out with JANA 2006.[24]

For dc magnetic susceptibility and isothermal magnetization measurements, a Quantum Design Physical Property Measurement System (QD-PPMS) was used in the range 4−350 K and for applied magnetic fields of ± 9T. Polycrystalline powders of $MnAs_{1-x}P_x$ were loaded into plastic holders clipped onto a brass half-tube sample holder and loaded into the cryostat of the VSM-based ACMS-II unit. For dc susceptibility measurements, static fields between 0.05 and 5 T were applied. In general, zero field cooled−warming (ZFC), field-cooled−cooling (FCC), and field-cooled−warming (FCW) cycles were followed. For dc isothermal magnetization measurements at selected temperatures, the magnetic field was ramped between 0 and ±9 T. For all measurements, samples were allowed substantial time to establish thermal equilibrium before measurements were started.

https://doi.org/10.1021/acs.chemmater.1c00128
Chem. Mater. 2021, 33, 2576−2584

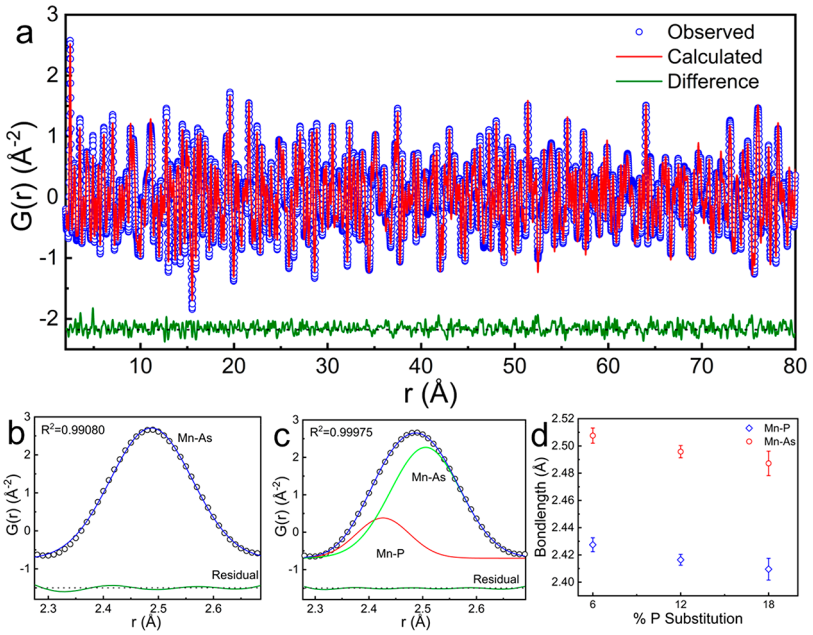

Figure 2. (a) PDF data for $MnAs_{0.94}P_{0.06}$ fitted in space group *Pnma*; a = 5.5338(1) Å, b = 3.4719(3) Å, and c = 6.1349(2) Å at 100 K (R_w = 15.6%). Blue open circles represent observed and red line represents calculated PDF based on the refinement, and green line shows the difference between observed and the calculated PDF. (b) First PDF peak (circles) and fit (blue solid line) with one Gaussian function, and green line shows residual of the fitting. (c) First PDF peak (circles) and fit (blue solid line) with two Gaussian functions shown in red and green. (d) Variation of the Mn−P (blue) and Mn−As (red) bond distances as a function of P substitution for $MnAs_{1-x}P_x$.

RESULTS AND DISCUSSION

Figure 1a shows the variable-temperature PXRD patterns for $MnAs_{0.94}P_{0.06}$ and a zoomed-in view (Figure 1b) of the main peak that illustrates the continuous orthorhombic (O; MnP-PM) to hexagonal (H; NiAs-PM) phase transition. At 100 K, $MnAs_{0.94}P_{0.06}$ crystallizes in the orthorhombic space group *Pnma* and undergoes an ASPT to a hexagonal phase ($P6_3/mmc$). The respective unit cells are related by $\mathbf{a}_O = \mathbf{c}_H$, $\mathbf{b}_O = \mathbf{b}_H$, and $\mathbf{c}_O = 2\mathbf{b}_H + \mathbf{a}_H$, implying that $|\sqrt{3} - \mathbf{c}_O/\mathbf{b}_O|$ is a measure of the distortion, although not being a good order parameter for the transition. The PXRD clearly shows that the ASPT occurs over a temperature range of some 200 K, where a gradual transition from the orthorhombic structure to the hexagonal structure occurs. From Figure 1 we note that, e.g., the orthorhombic $(102)_O$ and $(111)_O$ peaks at around 8.7° and 8.8° merge into $(101)_H$ on heating. Further orthorhombic $(210)_O$ and $(112)_O$ peaks at around 10.7° and 11° disappear only after 400 K. Reciprocal space Rietveld refinements were carried out for the composition $MnAs_{0.94}P_{0.06}$ at all temperatures. A single orthorhombic phase could be fitted to data until a temperature of 400 K (see Figures S1−S3 and Table S1). At 425 K, phase fractions were 68.34% and 31.66% for orthorhombic and hexagonal phases, respectively. Beyond 425 K, only the hexagonal phase could be fitted to the data. Phase fraction obtained from Rietveld refinement might be misleading since there are overlapping Bragg peaks from both phases. Therefore, these Rietveld refinements could not establish the true nature of the phase transition. In these circumstances, real-space PDF refinement is advantageous to determine the phases fraction. A similar problem of overlapping Bragg peaks was observed in the case of intermetallic PtGd structure determination. Real-space PDF refinement established that the real structure crystallizes in the space group *Pm*-3*m* instead of *Fm*-3*m* determined from Rietveld refinement.[25] The PXRD data reveals that the ASPT depends strongly on composition (x) (see Supporting Information (SI) Figures S4 and S5). These observations are well in line with earlier studies as well as paramagnetic scattering data.[20]

A pertinent question is now whether changes in the local coordination starts to take place prior to the crystallographically averaged structural transition as revealed by the PXRD data. At the local scale it might well be possible that there exist islands of hexagonal symmetry emerging in the orthorhombic matrix owing to compositional fluctuations and/or slight atomic rearrangements.

A detailed analysis of the local and intermediate-range structures was carried out based on PDF data in real space. Figure 2a shows the PDF data of $MnAs_{0.94}P_{0.06}$ at 100 K fitted in *Pnma* (R_w = 15.6%) for the r range 2−80 Å. The presence of two different bond distances due to Mn−As and Mn−P local environments were investigated by a detailed analysis of the first peak at 2.48 Å, which corresponds to the first neighbor distances of Mn, i.e., the $Mn(As,P)_6$ octahedron. Attempting a fit with one Gaussian peak was unsatisfactory, Figure 2b. However, for the choice of two Gaussian peaks (Figure 2c), the fit improved significantly, and the derived distances of 2.507(1) and 2.426(1) Å are attributed to Mn−As and Mn−P bonds, respectively. Similarly, two Gaussian peaks were found to improve the fitting of the first peak in all other data sets in all compositions (see Figures S6−S8) until the temperature where there was no change in the local structure (discussed later). Therefore, we have direct intuitive evidence of two distinct bond distances, which implies that the situation in MnP and MnAs is transferred into the local structure of the solid solution phase. Figure 2d shows the variation of these two bond distances with respect to P substitution. The assigned Mn−P bond distance shifts toward a lower value on increasing P substitution (x), whereas the Mn−As distance shifts toward longer distance on increasing As content, approaching those of MnAs (average Mn−As bond = 2.58 Å for MnAs; average

https://doi.org/10.1021/acs.chemmater.1c00128
Chem. Mater. 2021, 33, 2576−2584

Mn−P bond = 2.36 Å for MnP). Cell parameters and the average bond distance Mn−As/P decrease with increasing P substitution following Vegard's Law. These variations suggest that the electronic state of the M atoms changes within the analyzed composition interval at room temperature. As expected, the area under Mn−P bond distances increases while the area under Mn−As peak decreases with increasing P substitution (see Figure S10). It shows qualitatively that the area under the Mn−P peak increases with increasing P substitution without considering the scattering intensity of the atoms and normalizing them with respect to the scattering intensity. Further concentration dependence of the peak widths to separate the broadening due to static atom displacements from the thermal broadening was also not considered. Therefore, the area under the peak might be overestimated. When different sized atoms are substituted in the same crystal lattice, it is expected to have different bond distances. For example, in the case of $Ga_{1-x}In_xAs$, high-resolution PDF data clearly shows two very distinctive peaks corresponding to In−As and Ga−As at 2.65 and 2.45 Å, respectively.[26] Two Gaussian peaks were used to fit these peaks to find out the corresponding bond distances. Two peaks were clearly resolved because of the high-resolution data (Q_{max} = 45 $Å^{-1}$). Further, with increasing In substitution, the In−As peak intensity increases while the Ga−As peak intensity decreases. Similarly, when a smaller atom, here P in place of As, is substituted in MnAs, this is expected to give rise to two different bond distances corresponding to Mn−As and Mn−P. However, more high-resolution data are required to quantitatively show the trend by Gaussian fitting well-separated peaks by considering instrument broadening. The resolution of PDF is defined by π/Q_{max}, and we used a Q_{max} of 28 $Å^{-1}$. Therefore, a shoulder is observed corresponding to the Mn−P bond left side of the Mn−As bond distance.

In order to clarify local departures from the average picture provided by Bragg diffraction, PDF refinements were carried out for a local structure confined to the r range 2−20 Å and an intermediate-range structure for the r range 20−80 Å. At temperatures below 175 K, the local PDF structure was satisfactorily described based on the orthorhombic structure (R_w = 10.5% for $MnAs_{0.94}P_{0.06}$). At 175 K and higher temperatures, this type of fit (*Pmna*) leads to increasing values for R_w, Figure 3a. However, when adding a local component with a hexagonal structure to the refinement, the fit improved significantly. Figure 3a shows the variation of R_w with temperature. Hence, there are indications of a change in the local structure already at 175−200 K. At this temperature hexagonal domains appear locally. However, the average structure remains orthorhombic as shown by the diffraction data with a transition temperature of 425 K. On the other hand, the PDF intermediate-range picture (20−80 Å) indicates a decrease in the phase fraction of orthorhombic domains above 275 K, Figure 3b. To investigate the dependency of the hexagonal domain in orthorhombic matrix, PDF refinement was carried out with different r ranges. When the PDF refinement was restricted to the r range of 2−10 Å, there was no significant difference observed in the phase fractions compared to an r range of 2−20 Å. When the refinement range was increased to 2−30 Å, the change in the local structure was observed between 200 and 225 K (Figure 3 b). This is in line with the change in the intermediate-range structure (20−80 Å) where the change occurs beyond 275 K. Interestingly, although PXRD (average structure) suggests that the structural phase

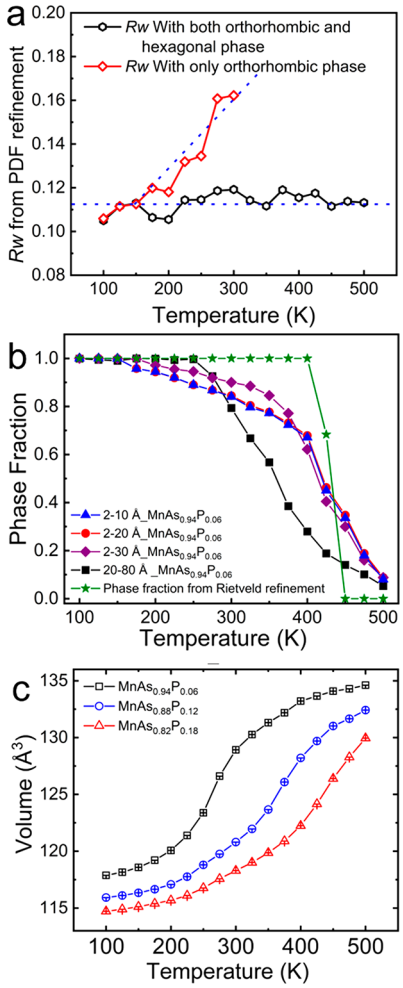

Figure 3. (a) R_w for refinements of the local (2−20 Å) structures of $MnAs_{0.94}P_{0.06}$ as a function of temperature. Red squares represent R_w with only the orthorhombic phase fitted, and black hexagons represent R_w with both the orthorhombic phase and the hexagonal included in the refinement. (b) Orthorhombic phase fraction of the local (2−10 Å, blue triangles; 2−20 Å, red circles; 2−30 Å, purple diamonds) and intermediate range structures (20−80 Å; black squares) of $MnAs_{0.94}P_{0.06}$. Green stars represent the phase fraction obtained from Q space Rietveld refinement. (c) Temperature-induced changes in the unit cell volume for the orthorhombic phase: (squares) $MnAs_{0.94}P_{0.06}$, (circles) $MnAs_{0.88}P_{0.12}$; (triangles) $MnAs_{0.82}P_{0.18}$.

transition is complete at 425 K, the PDF refinement indicates that orthorhombic domains prevail even up to around 500 K. A similar behavior was found for the more P-rich compositions: $MnAs_{0.88}P_{0.12}$ and $MnAs_{0.82}P_{0.18}$. For these, the onset of changes in the local structure (i.e., two-phase model required) is around 225 and 250 K, respectively. However, for the latter samples, the orthorhombic phase is stabilized owing to the smaller unit cell volume imposed by the higher P content. Hence, the phase transition to hexagonal symmetry is not complete at neither the local nor the average scale at 500 K ($MnAs_{0.88}P_{0.12}$ orthorhombic = 10.5%; $MnAs_{0.82}P_{0.18}$ orthorhombic = 76.9%).

These findings corroborate the previous observation of the paramagnetic scattering, which proved the magnetic low- to high-spin transition took place over the same wide temperature range.[20] For the $MnAs_{1-x}P_x$ solid solution phase, the temperature-dependent structural deformations (ASPT) is accompanied by a change in the magnetic properties of

https://doi.org/10.1021/acs.chemmater.1c00128
Chem. Mater. 2021, 33, 2576−2584

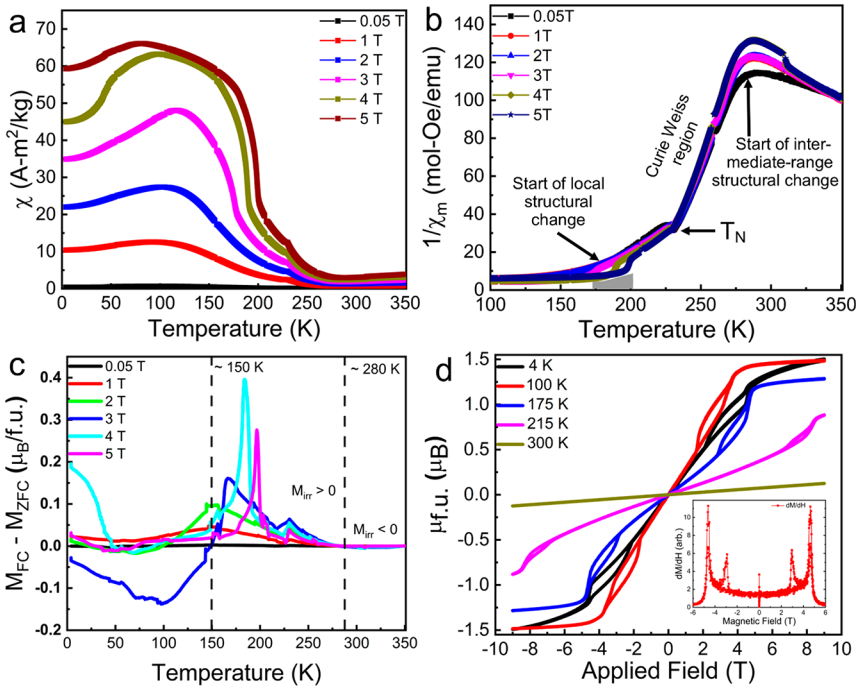

Figure 4. (a) Isofield magnetic ZFC susceptibility at various field strengths for $MnAs_{0.94}P_{0.06}$. (b) Isofield inverse magnetic susceptibility showing Curie−Weiss behavior in the limited range 232−275 K. (c) Irreversible susceptibility for different applied magnetic fields. (d) Isothermal magnetization $M(H)$ data showing saturation magnetization at high fields and a metamagnetic loop opening at intermediate fields. (Inset) Derivative of 100 K $M(H)$ data showing the sharpness of the transition.

manganese from a low-spin configuration (at 10 K) to a high-spin configuration (at 500 K). The complex magnetic and structural properties have a pronounced effect on heat capacity, which shows three major anomalies: spin disorder; low- to high-spin conversion, and structural phase transition (MnP−PM to NiAs−PM).[27,28] Susceptibility measurements do not give useful information in the temperature range for the low- to high-spin transition. However, from the observed Curie−Weiss relationship observed for the hexagonal high-temperature phase, the measured effective paramagnetic moment of μ_{eff} = 4.6 μ_B corresponds to S = 1.85 (spin-only approximation). The variation in S is well described based on paramagnetic scattering data.[20] The total scattering analysis indicates that there exist different structural domains, and the relative phase fraction is temperature dependent and correlates with the continuous spin transition at the average scale. A local high-spin situation is likely to be favored by a local hexagonal environment, whereas a local low-spin state is favored by a distorted orthorhombic environment. Although the emphasis is made synthetically to achieve a homogeneous solid solution by prolonged annealing, there will always exist different types of local coordination for the MnX_6 octahedra, i.e., $MnAs_6$, $MnAs_5P$, and $MnAs_4P_2$, but probably not more P-rich situations for a well-annealed sample in which compositional fluctuations are at a minimum. A high-spin situation will be most favored by $MnAs_6$ and least by $MnAs_4P_2$. Our current analysis shows that there is a gradual change in the phase fraction of two local structure regimes throughout the electronic and structural phase transitions. Further, the magnetic interaction between neighboring and next-nearest Mn dictates the continuous change in the paramagnetic moment. The local coordination around Mn, with its effect on interatomic Mn−(As, P) bond distances as well on Mn−Mn bond distances (and bond angles), plays a crucial role in determining the d orbital splitting, band broadening, positioning, and overlap, which results in either high-spin or low-spin situations in these metallic samples. Similar metal-to-metal interactions have been established for magnetite, Fe_3O_4, where local distortions occur due to magnetic ordering.[10] Upon warming through the Verwey transition at 125 K, the crystal structure of Fe_3O_4 changes from a monoclinic to a cubic inverse spinel structure. However, the monoclinic distortion persists in the local range (<10 Å) until the Curie temperature of 850 K. Here, fluctuations in the Fe−O−Fe bonding are the dominant instability that couples charge and orbital fluctuations to magnetic order. A somewhat related coexistence of nanoscale phases has been observed in the case of the metal−insulator transition in $Cu(Ir_{1-x}Cr_x)_2S_4$.[29]

Figure 3c shows the change in the unit cell volume of the orthorhombic phase (obtained from the intermediate-range structure PDF refinement) for all compositions as a function of temperature. The continuous volume change reiterates that the nature of the structural phase transition is second order.[19,20,30,31] There is an excellent agreement in the volume change for the local and intermediate-range structure descriptions for the orthorhombic phase (see SI, Figure S14). A similar good agreement is found for the unit cell volume of the hexagonal phase. The high uncertainty for the 175 K data point is attributed to the fact that this is the very first and weak appearance of the local hexagonal structure and corresponds to a nucleation process within an orthorhombic matrix. This parallels what is observed in the synthesis of nanoparticles. At very small particle sizes, nucleation is ongoing, the unit cell volume may deviate from that of larger crystalline particles, regular diffraction analysis is not applicable, and PDF analysis is required.[32,33] An anomaly in unit cell volume is also observed for the orthorhombic phase at 500 K, where the orthorhombic phase exists only locally, and

https://doi.org/10.1021/acs.chemmater.1c00128
Chem. Mater. 2021, 33, 2576−2584

uncertainty in the analysis becomes enhanced. Isotropic thermal parameters (U_{iso}) for both Mn and As increase with increasing temperature. However, a small change in slope can be seen in the temperature region 250−275 K, where the intermediate range structure starts to change (Figure S15). A similar change of slope in delta 2 is observed within this temperature window (Figure S16).

MAGNETIC PROPERTIES

The magnetic properties of $MnAs_{1-x}P_x$ are extraordinarily sensitive to changes in unit cell volume and interatomic distances, including chemical bonding. The reason is a volume-dependent low- to high-spin transition for the Mn atoms and changes in the Mn−Mn bonding as a result of the progressing structural phase transition. In this respect, the local structure is one more key parameter. However, individual effects are hard to separate. At low temperatures, where low-spin Mn is anticipated for the x = 0.06−0.18 samples, we nevertheless note a high complexity due to competing magnetic interactions. We illustrate this by data for x = 0.06. From earlier works, an antiferromagnetic double spiral H_a-type ordering was proved by single-crystal neutron diffraction for $MnAs_{0.925}P_{0.075}$,[34] whereas powder neutron diffraction (PND) showed that the H_a helimagnetic structure disappears at fields above 1 T. However, the emergence of new magnetic peaks is indicative of a different incommensurate structure with long periodicity. For $MnAs_{0.90}P_{0.10}$, PND shows that ferromagnetism occurs in an intermediate temperature range, with H_a order below and above, whereas $MnAs_{0.82}P_{0.18}$ is fully ferromagnetic below T_C[31] with a moment of 1.46 μ_B aligned along [010].[19] For H_a, the spins rotate in the bc plane (easy plane of magnetization in MnAs) with spiral propagation along [100] (hard axis). Early works show clearly that sample quality (annealing conditions) has a significant impact on measured magnetic features. This is likely caused by differences in the local structure and local clustering as revealed in the current PDF study, even for long-term annealed samples, with implications for spin transitions and magnetic short- and long-range interactions.

The isothermal magnetization data, exemplified with $MnAs_{0.94}P_{0.06}$, see Figure 4 d, document this complexity. Except for the paramagnetic state at 300 K, the $M(H)$ curves show a hysteresis loop at intermediate (2−8 T) fields. These features, not earlier clearly revealed, indicate a field-induced magnetic state, which indeed could represent the mentioned field-induced incommensurate structure. At high fields, the helical state transforms into a commensurate ferromagnetic (FM) state, $\mu_{sat} \approx 1.50\ \mu_B$/fu ($x$ = 0.06). In very high pulsed fields up to 30 T, a discontinuous volume expansion occurs caused by a first-order magnetic phase transition from the (low-spin) MnP type to the (high-spin) NiAs type along with a transition from para/heli- to ferromagnetism.[35] This transition exhibits similar ΔV and ΔS as reported for binary MnAs and is interesting as a magneto/barocaloric system.[18]

The isofield susceptibilities, Figure 4a and 4b, show complex behavior both below and above the ordering temperatures. The existence of a field-induced intermediate (probably incommensurate) magnetic state is evidenced also by the inverse susceptibility data (Figure 4 b; highlighted in gray), where the field-induced transition shifts from ∼165 K at 3 T to ∼200 K at 5 T. Further insight into the effect of the external field is provided in Figure 4c, showing the temperature dependence of irreversible susceptibility, $M_{irr} = M_{FC} - M_{ZFC}$ for samples measured in different fields on heating. The positive M_{irr} below $T_N \approx 230$ K indicates stabilization of field-nucleated collinear ferromagnetic (FM) phase. The noticeable M_{irr} peaks suggest that $MnAs_{0.94}P_{0.06}$ is subject to competing interactions between a magnetic incommensurate AFM helicoidal phase and a ferromagnetic phase where the energy balance is dictated by the strength of the applied magnetic field. In the narrow interval, 230−275 K, the inverse susceptibility (μ_0H = 0.05 T) follows the Curie−Weiss law with an effective paramagnetic magnetic moment of 2.01 μB and θ_{CW} = +215 K, indicating ferromagnetic interactions. The μ_{eff} corresponds to $2S \approx 1.5$, in line with the observed ordered moments and the claim of low-spin Mn (III). The anomalous $1/\chi(T)$ behavior at higher temperatures in Figure 4b is caused by the low- to high-spin continuous spin conversion during which we currently observe major changes in the local and intermediate-range structure, while a regular Curie−Weiss region again occurs in the hexagonal NiAs-type high-temperature phase (not shown). Corresponding data for $MnAs_{0.88}P_{0.12}$ and $MnAs_{0.82}P_{0.18}$ are shown in the SI.

The total scattering analysis reveals structural changes, locally and on intermediate range, in the temperature range of magnetic anomalies and phase transitions as well in connection with the major changes in susceptibility related to the low- to high-spin conversion. The local spin interactions between Mn atoms are susceptible to local distortions that are expectedly manifested by diffuse scattering and correlate with current findings of the TS analysis. A similar behavior is observed for all samples. A small unit cell volume per formula unit favors low spin rather than high spin. Magnetic analysis (neutron diffraction, saturation magnetization, CW regimes) documents the spin situation at certain conditions. In this context, the current PDF data adds insight to the paramagnetic low- to high-spin transition that couples to the second-order structural phase transition (from *Pnma* to $P6_3/mmc$). The best data for the variation of the spin moment is assumingly obtained from paramagnetic neutron scattering.[20] In Figure 5 we plot how this derived spin moment S correlates with the average Mn−P/As bond distances of the octahedra in the composite mixture of orthorhombic and hexagonal phases, as revealed by TS analysis. The kink in the scattering data at ca. 230 K corresponds to the magnetic ordering transition.

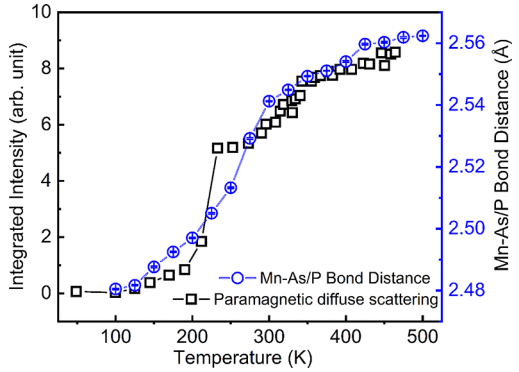

Figure 5. Correlation of average Mn−As/P bond distances (blue circles) derived from PDF refinement with paramagnetic diffuse scattering (black squares) versus temperature for $MnAs_{0.94}P_{0.06}$. Paramagnetic scattering results were reproduced from a published article.[20]

https://doi.org/10.1021/acs.chemmater.1c00128
Chem. Mater. 2021, 33, 2576−2584

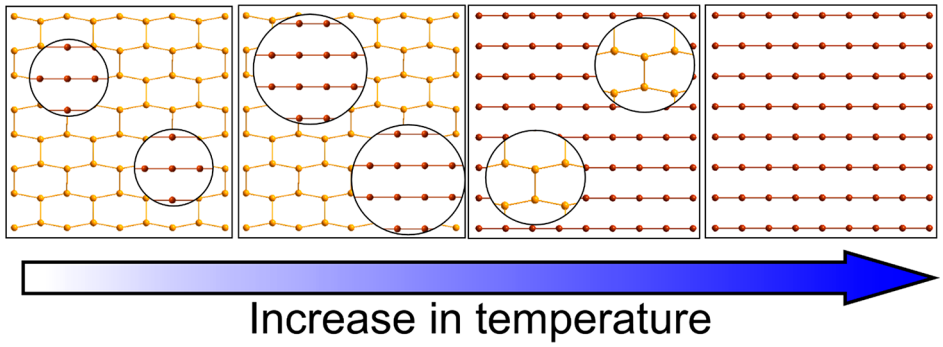

Figure 6. Zig-zag Mn−Mn chain arrangement along *a* in the orthorhombic (yellow spheres) structure viewed along the *b* axis with the island of a NiAs-like local order in terms of a linear chain of Mn atoms (brown sphere) representing hexagonal symmetry. With increasing temperature the local hexagonal islands grow within the orthorhombic matrix and finally transform into a complete hexagonal structure.

DISCUSSION AND CONCLUSION

When exploring a solid solution, as currently exemplified by the pseudobinary $MnAs_{1-x}P_x$ phase, one will synthetically normally strive for maximum homogeneity at all length scales and thereby be able to fully study in detail how the physicochemical properties vary with parameters like the average electronegativity, electron concentration, chemical pressure, charge states, and more. For certain materials systems, the effect of tuning chemical substitution has a pronounced effect on the structure and properties. This is indeed the case for $MnAs_{1-x}P_x$, where the Mn electronic state and thereby the "atomic size" (unit cell volume; symmetry) are sensitive parameters to be tuned and explored.

The current total scattering analysis shows that the individual Mn−As and Mn−P bonds differ significantly in lengths, as one may expect from simple atomic size arguments. However, since a given nonmetal atom (P, As) in the NiAs-type and the distorted MnP-type structures connects to six Mn atoms (octahedra), displacements/deformations and strain are very likely to occur at the local scale. In an ionic picture, this will lead to different local crystal fields with an impact on the d-electron levels. In metallic $MnAs_{1-x}P_x$, the orthorhombic distortion directly leads to the establishment of new metal−metal interactions (bonds) and to changes in the DOS at the Fermi level, including spin-up and spin-down bands. These changes correspond in the ionic limit to a low- ($S = 1$) to high-spin ($S = 2$) transition. The structural implication of islands with NiAs-like local structure in a matrix of deformed MnP-type is visualized in Figure 6. This corresponds to the current findings in the PDF analysis of the paramagnetic phase that undergoes a low- to high-spin transition.

The total scattering analyses reveal interesting features connected with temperature-induced electronic and structural phase transitions. The high-spin state is governed by high local symmetry; there are no metal atom displacements that would impose new metal−metal bonds (in the *ac* plane; *Pnma*) and a large local volume for the Mn coordination polyhedron (i.e., Mn−As rather than Mn−P coordination). The current data indicates that nanodomains develop in the structural transition region. There appear to be domains of higher symmetry (modeled as NiAs-type arrangement) along with orthorhombic domains. Such a coexistence model was required to obtain acceptable fits of the TS data in the transition regions. On average, this translates nicely into a continuous $V(T)$ thermal expansion relation with a maximum in thermal expansivity in the temperature range where the total scattering data shows the largest difference between local (<20 Å) and intermediate-range (20−80 Å) structures. This is consistent with the continuous variation in the displacement (and order) parameter $|1/4 - z_{Mn}|$ (being a measure of new Mn−Mn "bonds" formed) as as revealed from variable-temperature neutron diffraction studies.[19] The observed temperature-induced changes in the local structure are very similar for all three investigated samples of $MnAs_{1-x}P_x$ ($x = 0.06, 0.12, 0.18$) and hence probably of quite generic validity. The electronic low- to high-spin transition takes place over a large temperature interval. We suggest that this is indeed due to the existence of a wide distribution of local coordinations for the Mn atoms with respect to the nearest and next-nearest neighbor P and As atoms. Hence, we immediately recognize that sample homogeneity is essential for structural and electronic properties. Only a homogeneous sample at all length scales will give sharp DSC (differential scanning calorimetry) signals for the enthalpy changes of relevant transitions. The $MnAs_{1-x}P_x$ system is extraordinary by showing an unusually strong coupling between local structure, average structure, and magnetism. It is therefore very well suited for exploring phenomena that otherwise easily escape detection yet being of high generic importance for solid solutions and materials science.

The current studies, as well as the literature, suggest a thermodynamically second-order phase transition. Pure structural MnP- to NiAs-type transitions are known for, e.g., CrAs with no coupling to any magnetic transition. The situation for Mn−As-P is significantly different since the temperature-induced changes in the average unit cell volume correlate with a conversion from a low- to a high-spin situation for the Mn atoms. In this respect, the local symmetry and the local Mn−(P, As) distances/environment become a real factor for spin conversion and probably also for the structural phase transition. An intriguing question is what drives the second-order phase transition in this system. Parameters like impurities, strain, and grain boundaries could impact the transition. However, care has been taken to minimize these potential parameters in the synthesis; using ultrapure elements as reactants and repeated crushing and long-term annealing are conducted to achieve a high level of P, As homogeneity. The sluggishness of the phase transition allowed us to probe the local picture. PDF analysis indicates that the material is not uniform during the phase transition. Locally some Mn−As-P atoms arrange themselves in a hexagonal-like manner while others remain in an orthorhombic arrangement. In a solid solution, there will be certain distributions of the atoms at the

https://doi.org/10.1021/acs.chemmater.1c00128
Chem. Mater. 2021, 33, 2576−2584

local level. In the NiAs-type structure, Mn sits in octahedral (P, As) coordination with 6 + 2 Mn next-nearest neighbors. Each P, As bonds to six Mn neighbors (trigonal prismatic coordination). Therefore, the local structure of the Mn−$(P, As)_6$ octahedra will depend on the level of the P substitution and the distortion relative to the next-nearest metal atom neighbors. PDF indicates that these distorted octahedra behave differently on heating the material. Some remain distorted, probably due to their vicinity to P atoms and possibly also grain boundaries. Other octahedra change their spin and turn into a high-spin local situation which requires a simultaneous increase in the local symmetry. An interesting question is whether similar features can occur for other solid solution phases that undergo second-order phase transitions. These findings are interesting and provide new insight into phase transition. This brings about a tantalizing possibility where one could imagine phase transitions not as globally abrupt and/or starting and finishing where major entropy changes start and stop but rather as coexisting local structures competing energetically for dominance.

■ ASSOCIATED CONTENT

Supporting Information

The Supporting Information is available free of charge at https://pubs.acs.org/doi/10.1021/acs.chemmater.1c00128.

Rietveld refinement parameters and pattern for $MnAs_{0.94}P_{0.06}$; atomic coordinates obtained from both PDF and Rietveld refinement; variable-temperature PXRD of $MnAs_{0.88}P_{0.12}$ and $MnAs_{0.82}P_{0.18}$; Gaussian peak fitting of the first PDF peak of all three compositions and silicon; variation of the normalized area under the individual peak of Mn−P and Mn−A; variation of cell parameters and bond lengths with respect to P substitution; fitted PDF pattern at 175 and 250 K with both hexagonal and orthorhombic phase; comparison of volume change in PDF refinement between local and intermediate-range structure; isotropic thermal parameter and delta2 variation with temperature; phase fraction of the orthorhombic structure at local and intermediate-range structure; magnetic data for $MnAs_{0.88}P_{0.12}$ and $MnAs_{0.82}P_{0.18}$ (PDF)

■ AUTHOR INFORMATION

Corresponding Authors

Dipankar Saha − *Center for Materials Science and Nanotechnology, Department of Chemistry, University of Oslo, N-0315 Oslo, Norway;* orcid.org/0000-0002-2197-2568; Email: dipankar.saha@smn.uio.no

Helmer Fjellvåg − *Center for Materials Science and Nanotechnology, Department of Chemistry, University of Oslo, N-0315 Oslo, Norway;* orcid.org/0000-0001-6045-7211; Email: helmer.fjellvag@kjemi.uio.no

Authors

Susmit Kumar − *Center for Materials Science and Nanotechnology, Department of Chemistry, University of Oslo, N-0315 Oslo, Norway*

Bruno Gonano − *Center for Materials Science and Nanotechnology, Department of Chemistry, University of Oslo, N-0315 Oslo, Norway;* orcid.org/0000-0002-7331-2131

Anja Olafsen Sjåstad − *Center for Materials Science and Nanotechnology, Department of Chemistry, University of Oslo, N-0315 Oslo, Norway*

Complete contact information is available at: https://pubs.acs.org/10.1021/acs.chemmater.1c00128

Author Contributions

D.S. and H.F. designed and directed the study. D.S. synthesized the samples. D.S., B.G., and S.K. carried out total scattering experiments. D.S. and S.K. conducted magnetic measurements. D.S., S.K., and H.F wrote the manuscript with the contributions of all coauthors. All authors have given approval to the final version of the manuscript.

Funding

We acknowledge financial support by the Research Council of Norway under the FRIPRO project NAMM/144590

Notes

The authors declare no competing financial interest.

■ ACKNOWLEDGMENTS

We acknowledge financial support by the Research Council of Norway under the FRIPRO project NAMM/144590. The authors thank the Swiss Light Source, Paul Scherrer Institut for beamtime. We also thank Dr. Antonio Cervellino for all the help during beamtime.

■ REFERENCES

(1) Dagotto, E. *Nanoscale phase separation and colossal magnetoresistance: the physics of manganites and related compounds*; Springer Science & Business Media, 2013; Vol. *136*.

(2) Zorko, A.; Adamopoulos, O.; Komelj, M.; Arčon, D.; Lappas, A. Frustration-induced nanometre-scale inhomogeneity in a triangular antiferromagnet. *Nat. Commun.* **2014**, *5*, 3222.

(3) Glasbrenner, J.; Mazin, I.; Jeschke, H. O.; Hirschfeld, P.; Fernandes, R.; Valentí, R. Effect of magnetic frustration on nematicity and superconductivity in iron chalcogenides. *Nat. Phys.* **2015**, *11*, 953.

(4) Borisenko, S.; Kordyuk, A.; Yaresko, A.; Zabolotnyy, V.; Inosov, D.; Schuster, R.; Büchner, B.; Weber, R.; Follath, R.; Patthey, L.; et al. Pseudogap and charge density waves in two dimensions. *Phys. Rev. Lett.* **2008**, *100*, 196402.

(5) Frandsen, B. A.; Gong, Z.; Terban, M. W.; Banerjee, S.; Chen, B.; Jin, C.; Feygenson, M.; Uemura, Y. J.; Billinge, S. J. L. Local atomic and magnetic structure of dilute magnetic semiconductor $(Ba,K)(Zn,Mn)_2As_2$. *Phys. Rev. B: Condens. Matter Mater. Phys.* **2016**, *94*, 094102.

(6) Orenstein, J.; Millis, A. Advances in the physics of high-temperature superconductivity. *Science* **2000**, *288*, 468−474.

(7) Zhang, J.; Ding, Z.; Tan, C.; Huang, K.; Bernal, O. O.; Ho, P.-C.; Morris, G. D.; Hillier, A. D.; Biswas, P. K.; Cottrell, S. P.; Xiang, H.; Yao, X.; MacLaughlin, D. E.; Shu, L. Discovery of slow magnetic fluctuations and critical slowing down in the pseudogap phase of $YBa_2Cu_3O_y$. *Science Advances* **2018**, *4*, No. eaao5235.

(8) Campbell, I.: Magnetic Systems: Disordered. In *Encyclopedia of Materials: Science and Technology*; Buschow, K. H. J., Cahn, R. W., Flemings, M. C., Ilschner, B., Kramer, E. J., Mahajan, S., Veyssière, P., Eds.; Elsevier: Oxford, 2001; pp 4969−4976.

(9) Egami, T.; Billinge, S. J. *Underneath the Bragg Peaks: Structural Analysis of Complex Materials*; Pergamon, 2012; Vol. *16*.

(10) Perversi, G.; Pachoud, E.; Cumby, J.; Hudspeth, J. M.; Wright, J. P.; Kimber, S. A.; Attfield, J. P. Co-emergence of magnetic order and structural fluctuations in magnetite. *Nat. Commun.* **2019**, *10*, 2857.

(11) Wang, Y.; Feng, Y.; Cheng, J. G.; Wu, W.; Luo, J. L.; Rosenbaum, T. F. Spiral magnetic order and pressure-induced

superconductivity in transition metal compounds. *Nat. Commun.* **2016**, *7*, 13037.
(12) Park, S.; Shin, S.; Kim, S.-I.; Kim, S.; Park, C.-K.; Thompson, J. D.; Park, T. Tunable quantum critical point and detached superconductivity in Al-doped CrAs. *npj Quantum Mater.* **2019**, *4*, 49.
(13) Smith, A.; Bahl, C. R.; Bjørk, R.; Engelbrecht, K.; Nielsen, K. K.; Pryds, N. Materials challenges for high performance magnetocaloric refrigeration devices. *Adv. Energy Mater.* **2012**, *2*, 1288−1318.
(14) Franco, V.; Blázquez, J.; Ingale, B.; Conde, A. The magnetocaloric effect and magnetic refrigeration near room temperature: Materials and models. *Annu. Rev. Mater. Res.* **2012**, *42*, 305−342.
(15) Krenke, T.; Duman, E.; Acet, M.; Wassermann, E. F.; Moya, X.; Mañosa, L.; Planes, A. Inverse magnetocaloric effect in ferromagnetic Ni-Mn-Sn alloys. *Nat. Mater.* **2005**, *4*, 450.
(16) Tegus, O.; Brück, E.; Buschow, K.; De Boer, F. Transition-metal-based magnetic refrigerants for room-temperature applications. *Nature* **2002**, *415*, 150.
(17) Wada, H.; Taniguchi, K.; Tanabe, Y. Extremely large magnetic entropy change of MnAs1-xSbx near room temperature. *Mater. Trans.* **2002**, *43*, 73−77.
(18) Łażewski, J.; Piekarz, P.; Parlinski, K. Mechanism of the phase transitions in MnAs. *Phys. Rev. B: Condens. Matter Mater. Phys.* **2011**, *83*, 054108.
(19) Fjellvåg, H.; Andresen, A. F.; Bärner, K. On the magnetic and structural properties of the $MnAs_{1-x}P_x$ system (x-0.18). *J. Magn. Magn. Mater.* **1984**, *46*, 29−39.
(20) Andresen, A. F.; Fjellvåg, H.; Steinsvoll, O.; Kjekshus, A.; Stølen, S.; Bärner, K. Paramagnetic scattering experiments on $MnAs_{1-x}P_x$, x = 0.06, 0.12 and 0.18. *J. Magn. Magn. Mater.* **1986**, *62*, 241−246.
(21) Willmott, P.; Meister, D.; Leake, S.; Lange, M.; Bergamaschi, A.; Böge, M.; Calvi, M.; Cancellieri, C.; Casati, N.; Cervellino, A.; et al. The materials science beamline upgrade at the Swiss Light Source. *J. Synchrotron Radiat.* **2013**, *20*, 667−682.
(22) Juhás, P.; Davis, T.; Farrow, C. L.; Billinge, S. J. PDFgetX3: a rapid and highly automatable program for processing powder diffraction data into total scattering pair distribution functions. *J. Appl. Crystallogr.* **2013**, *46*, 560−566.
(23) Yang, X.; Juhas, P.; Farrow, C. L.; Billinge, S. J. xPDFsuite: An end-to-end software solution for high throughput pair distribution function transformation, visualization, and analysis. arXiv:1402.3163; https://arxiv.org/abs/1402.3163 (accessed 2020-08-20.
(24) Petžíček, V.; Dušek, M.; Palatinus, L. Crystallographic computing system JANA2006: general features. *Z. Kristallogr, Cryst Mater.* **2014**, *229*, 345−352.
(25) Saha, D.; Bøjesen, E. D.; Jensen, K. M. ø.; Dippel, A.-C.; Iversen, B. B. Formation mechanisms of Pt and Pt_3Gd nanoparticles under solvothermal conditions: An in situ total X-ray scattering study. *J. Phys. Chem. C* **2015**, *119*, 13357−13362.
(26) Petkov, V.; Jeong, I. K.; Chung, J. S.; Thorpe, M. F.; Kycia, S.; Billinge, S. J. L. High real-space resolution measurement of the local structure of $Ga_{1-x}In_xAs$ using X-Ray diffraction. *Phys. Rev. Lett.* **1999**, *83*, 4089−4092.
(27) Labban, A. K.; Westrum Jr, E. F.; Fjellvåg, H.; Grønvold, F.; Kjekshus, A.; Stølen, S. Heat capacity of $MnAs_{0.88}P_{0.12}$ from 10 to 500 K: Thermodynamic properties and transitions. *J. Solid State Chem.* **1987**, *70*, 185−198.
(28) Krokoszinski, H. J.; Santandrea, C.; Gmelin, E.; Bärner, K. Specific heat anomaly connected with a High-Spin-Low-Spin transition in metallic $MnAs_{1-x}P_x$ crystals. *Phys. Status Solidi B* **1982**, *113*, 185−195.
(29) Božin, E. S.; Knox, K. R.; Juhás, P.; Hor, Y. S.; Mitchell, J. F.; Billinge, S. J. L. $Cu(Ir_{1-x}Cr_x)_2S_4$: A model system for studying nanoscale phase coexistence at the metal-insulator transition. *Sci. Rep.* **2015**, *4*, 4081.
(30) Suzuki, T.; Ido, H. Relation between Structural and Magnetic Properties of Compound $MnAs_{1-x}P_x$ (0-x-0.275). *J. Phys. Soc. Jpn.* **1982**, *51*, 3149−3156.
(31) Fjellvåg, H.; Kjekshus, A.; Stølen, S. Structural and magnetic properties of $MnAs_{0.90}P_{0.10}$. *J. Solid State Chem.* **1986**, *64*, 123−133.
(32) Bøjesen, E. D.; Iversen, B. B. The chemistry of nucleation. *CrystEngComm* **2016**, *18*, 8332−8353.
(33) Saha, D.; Bøjesen, E. D.; Mamakhel, A. H.; Iversen, B. B. Why does Bi_2WO_6 visible-light photocatalyst always form as nanoplatelets? *Inorg. Chem.* **2020**, *59*, 9364−9373.
(34) Haneda, S.; Kazama, N.; Yamaguchi, Y.; Watanabe, H. Electronic State of Low Spin MnAs(P). *J. Phys. Soc. Jpn.* **1977**, *42*, 1212−1220.
(35) Kido, G.; Ido, H. Forced magnetostrictions on $MnAs_{1-x}P_x$ (x < 0.275) under pulsed magnetic field up to 300 kOe. *J. Magn. Magn. Mater.* **1987**, *70*, 207−208.

https://doi.org/10.1021/acs.chemmater.1c00128
Chem. Mater. 2021, 33, 2576−2584